npj | climate and atmospheric science

www.nature.com/npjclimatsci

ARTICLE OPEN

Check for updates

What controls the interannual variation of Hadley cell extent in the Northern Hemisphere: physical mechanism and empirical model for edge variation

Kyong-Hwan Seo[1,2,3]✉, Sang-Pil Yoon[1,3], Jian Lu[4], Yongyun Hu[5], Paul W. Staten[6]✉ and Dargan M. W. Frierson[7]

The Hadley circulation is the most prominent atmospheric meridional circulation, reducing the radiatively driven equator-to-pole temperature gradient. While the Hadley cell extent varies by several degrees from year to year, the detailed dynamical mechanisms behind such variations have not been well elucidated. During the expanded phase of the Hadley cell, many regions on the periphery of the subtropics experience unfavorable climatic conditions. In this study, using ERA5 reanalysis data, we examine the physical chain of events responsible for the interannual variation of the Hadley cell edge (HCE) latitude in the Northern Hemisphere. This variation is mainly caused by changing eddy activity and wave breaking from both stationary and transient waves. In particular, we show that transient waves cause the HCE to shift poleward by increasing the eddy momentum flux divergence (EMFD) and reducing the baroclinicity over 20°–40°N, shifting the region of peak baroclinicity poleward. El Niño/La Niña and the Arctic Oscillation (AO) account for a significant portion (60%) of the interannual fluctuation of the HCE latitude. Through the poleward displacement of eddy activity, La Niña and a positive AO state are associated with the poleward shift of the HCE. The analysis of 28 CMIP5 models reveals statistical relationships between EMFD, vertical shear, and HCE latitude similar to those observed.

npj Climate and Atmospheric Science (2023)6:204 ; https://doi.org/10.1038/s41612-023-00533-w

INTRODUCTION

The Hadley circulation is the most prominent meridional atmospheric circulation in the tropics. It transports energy and momentum to higher latitudes, reducing the equator-to-pole temperature gradient formed by radiative forcing and supplying a portion of the angular momentum required to maintain the midlatitude storm tracks. During the solstices, rising motion is concentrated over the intertropical convergence zone in the summer hemisphere's deep tropics[1], while pronounced sinking motion occurs over a zonal belt of high pressure and arid climate in the winter hemisphere's subtropics.

Recent analyses of observations have revealed a poleward expansion of the annual mean Hadley cell (HC) at a rate of 0.1°–2.0° per decade[2–6]. However, the expansion mostly occurs in the summer and autumn cells in both the Northern (NH) and Southern Hemispheres (SH)[7]. Studies show that the HC edge (HCE) is projected to shift poleward during the 21st century at a rate of 0.03°–0.2° per decade owing to anthropogenic global warming[6,8–10]. However, this expansion is only statistically significant over the SH, where year-to-year shifts are smaller, whereas the NH edge tends to remain within the bound of the larger natural variability even into the late 21st century.

The poleward expansion of the HC has profound effects on the regional weather and climate of the entire planet. This could include a recent increase in aridity in the American Southwest, Mediterranean Europe, and southern China in the NH[11–13] and a decrease in precipitation across southern Australia and southern Amazonia in the SH[7,14–16], though all of these effects require further investigation. The more frequent occurrence of heat waves over central and western Europe in recent years may be another consequence of the HC's expansion during boreal summer[6]. HC expansion also affects tropical cyclone tracks, as these can extend further poleward owing to the poleward bulge of the subtropical high[17]. Thus, the poleward expansion of the HC may increase social and economic damages associated with heat, drought, and tropical cyclones.

Changes in tropical or subtropical tropopause height, subtropical static stability (i.e., saturated adiabatic lapse rate), poleward temperature gradient, vertical stretching of baroclinic eddies, baroclinicity, and wave breaking have been proposed as possible internal factors that control the latitudinal variation of the HCE[5,6,9,11,18–24]. Most of these and other studies focus on mechanisms of forced expansion in response to greenhouse gas concentration increases, stratospheric ozone depletion, volcanic eruptions, and anthropogenic aerosol increases[11,25–30]. Fewer studies investigate HCE shifts from year to year.

El Niño–Southern Oscillation (ENSO) has been identified as a primary mode of climate variability shifting the HCE from year to year in observations[5,31,32] and model simulations[11,33]. Due to the enhanced heating over the equator, the subsequent increase in latitudinal temperature gradient across the subtropics, and the resulting strengthening of the subtropical jet via the thermal wind relationship[34], El Niño-like forcing induces HC contraction.

Hu et al.[35] demonstrated that the boreal spring Arctic Oscillation (AO), which is a latitudinal shift of atmospheric pressure between the Arctic and the midlatitudes of the North Pacific and North Atlantic and is known to be driven primarily by midlatitude eddies[36–39], is positively correlated with the HCE[40,41]. During the

[1]Department of Atmospheric Sciences, Division of Earth Environmental System, Pusan National University, Busan 46241, South Korea. [2]Research Center for Climate Sciences, Pusan National University, Busan 46241, South Korea. [3]Future Earth Research Institute, PNU JYS Science Academy, Pusan National University, Busan 46241, South Korea. [4]Pacific Northwest National Laboratory, Richmond, WA 99354, USA. [5]Department of Atmospheric and Oceanic Sciences, School of Physics, Peking University, Beijing 100871, China. [6]Department of Earth and Atmospheric Sciences, Indiana University Bloomington, Bloomington, IN 47405, USA. [7]Department of Atmospheric Sciences, University of Washington, Seattle, WA 98195, USA. ✉email: khseo@pusan.ac.kr; pwstaten@indiana.edu

positive phase of the AO, enhanced wave propagation from mid- to high-latitudes to lower latitudes, primarily over the North Atlantic, leads to a poleward HCE shift. However, there has been no exhaustive examination of the characteristics and processes underlying the interannual variation in the HCE.

In this study, we use 41 years of reanalysis and sea surface temperature data to investigate the physical mechanisms of the year-to-year variation in the NH HCE latitude and the impact of each of the above modes of variability. This research highlights the significance of both stationary and transient wave fluxes. Specifically, we show that transient waves shift the HCE poleward by reducing baroclinicity in the subtropics.

RESULTS

The role of stationary and transient waves in poleward HCE shifts

Since the meridional temperature contrast between the tropics and the poles is greatest in winter, the HC, eddy momentum flux (EMF), and eddy temperature flux peak during the winter. This paper focuses on the boreal winter season; a subsequent publication will discuss the austral winter case. This study also summarizes boreal summer HCE shifts (see Supplementary Figs. 2–7), which are broadly similar to the boreal winter case.

Here, the HCE latitude is defined as the first zero-crossing latitude of the mass streamfunction at 500 hPa[5,42–44] over the subtropical region bounded by 20°N and 40°N. Figure 1a depicts the December–January–February–March (DJFM) mean HCE latitude time series from 1979 to 2019 calculated from ERA5 output. The average HCE latitude is 28.4°, with a standard deviation of 0.6°. During the period examined, there is a poleward but statistically insignificant linear trend[45], indicating that the observed trend falls within the range of internal variability[5,10]. This is consistent with Hu et al.[7]'s analysis, in which the linear trends in the DJF mean HC width from all reanalysis data analyzed, including 20CR2, CFSR, ERA-interim, JRA55, MERRA2, NCEP1, and NCEP2, are statistically indistinguishable from zero. Also in agreement with previous findings[9,46], the HCE latitudinal variation is substantially correlated with that of the HC strength (estimated as the maximum streamfunction at 500 hPa[18]) with a correlation of −0.52.

The climatological Hadley circulation based on the mass streamfunction is shown in Fig. 1b, with ascent over [−10°S, 5°N] and downward motion over [15°N, 30°N], and the HCE at approximately 30°N. The high-minus-low HCE latitude year composite streamfunction (where the seven years with the most poleward and the seven with the most equatorward HCE latitudes are selected; see the METHODS for details; see Fig. 1b) is positive over the downward branch, indicating an expansion of the HC toward higher latitudes. Concurrently, the negative anomaly between 0° and 10°N indicates a narrowing of the upwelling[47]. Overall, the Hadley circulation weakens slightly, consistent with the known negative relationship[7,11] between width and strength, and the Ferrel cell becomes slightly, but statistically significantly, more intense.

To investigate the physical processes associated with the interannual variation in HCE, we first examine the pertinent zonal-mean momentum equation:

$$\left(f+\overline{\zeta}\right)[\overline{v}] = (1-Ro)f[\overline{v}] \approx S = \frac{1}{a\cos^2\varphi}\frac{\partial}{\partial\varphi}\left(\cos^2\varphi\overline{[u^*v^*]}\right), \quad (1)$$

where f and ζ represent the planetary vorticity and the vertical component of relative vorticity, respectively, a is radius of the Earth, φ is latitude, u and v are zonal and meridional winds, respectively, Ro is the local Rossby number (defined as $-\overline{\zeta}/f$), and S is the horizontal eddy momentum flux divergence (EMFD). S corresponds to the meridional convergence of the Eliassen–Palm (EP) flux, which is used for visualizing wave propagation and breaking. The asterisk represents zonal deviations of the 6-hourly u and v from their respective zonal means (denoted as $[\cdot]$), while the bar indicates time mean. Since Ro is very small[48] (i.e., >0.1) at the latitude of the poleward boundary of the HC, $\overline{v} \approx S/f$, which implies that HCE location is strongly correlated with the location of zero-crossing of EMFD, and hence with EMFD anomalies at this zero-crossing.

As suggested by the above equation, the EMFD is the determining factor for the HCE[35,49]. The EMFD climatology for 1979–2019 is presented in Supplementary Fig. 1. To compute the temporal variation of the EMFD around the HCE, a domain [400–200 hPa, 20°–35°N] is selected. As shown in Fig. 2a, the HCE latitudinal variation is significantly correlated with the EMFD ($r = 0.82$), with a higher EMFD resulting in a more northward HCE position. In addition, the interannual variations of both the stationary and the transient EMFD (Fig. 2b, c) correlate strongly with those of the HCE latitude, with a similar level of collinearity. This result contrasts with the interannual variation of the HC intensity, in which it is known that stationary waves play a dominant role[48]. Meanwhile, the correlation between the stationary and transient EMFD is comparatively weak (Fig. 2d).

The observed meridional wind field regressed onto the HCE latitude time series shown in Fig. 1a is displayed as shading in Fig. 2e. Figure 2f, g are the derived meridional winds from the stationary and transient EMFD forcing using Eq. (1), which are then regressed onto the HCE latitude time series. The contours in these figures represent the corresponding DJFM climatology. In Fig. 2e, positive anomalies (red) in the upper troposphere are observed at 20°–30°N, which is poleward of the climatological southerly wind by ~5–10°, indicating a northward expansion of the HC. The meridional wind anomalies computed from the stationary component of the EMFD (Fig. 2f) show the southerly flow anomaly, with the zero contour centered at ~33°N. In contrast, the outflow from the transient component of the EMFD (Fig. 2g) exhibits the stronger southerly anomaly, with an areal mean two times greater than its stationary counterpart; more importantly, the zero contour is located further north, at approximately 40°N. In summary, the transient wave is the primary influence, with a secondary, complimentary contribution from the stationary wave, for the meridional shift of the HCE.

Since the EP flux helps identify the locations of eddy generation, propagation, and breaking, the EP flux and its divergence are presented in Fig. 3a, b. As mentioned before, EMFD is the meridional component of the EP flux convergence. EP flux convergence indicates wave breaking, which in turn decreases baroclinicity. The wintertime stationary EP flux (Fig. 3a) is directed upward and equatorward from midlatitudes (in contrast, there are downward-directed vectors in the middle and lower troposphere over 40°–60°N, indicating that the stationary waves are not baroclinically generated). This flux combines with the poleward-directed flux emanating from the upper levels of the tropics to produce a convergence of EP flux over the subtropics. This anomalous convergence is located north of the climatological EP flux convergence (i.e., the dotted contours), indicating a northward shift in the positive EMFD, the EMFD zero-crossing, and the HCE. By contrast, the anomalous transient EP flux (Fig. 3b) develops predominantly in the lower troposphere of the extratropics, between 40°N to 65°N, indicating baroclinic wave growth. This wave flux is generally directed upward in the middle troposphere and equatorward in the upper troposphere, forming an anomalous EP flux convergence due to wave breaking[50], again north of the climatological convergence region. In this case, the boundary between the EP flux convergence and divergence regions shifts more to the north than in the stationary case, indicating that transient waves drive the HCE further north.

The greater role of transient waves can be verified using the meridional distribution of the EMFD (Fig. 3c) at 250 hPa. Black line shows the climatological field and blue and red lines represent the EMFD anomalies from stationary and transient waves, respectively,

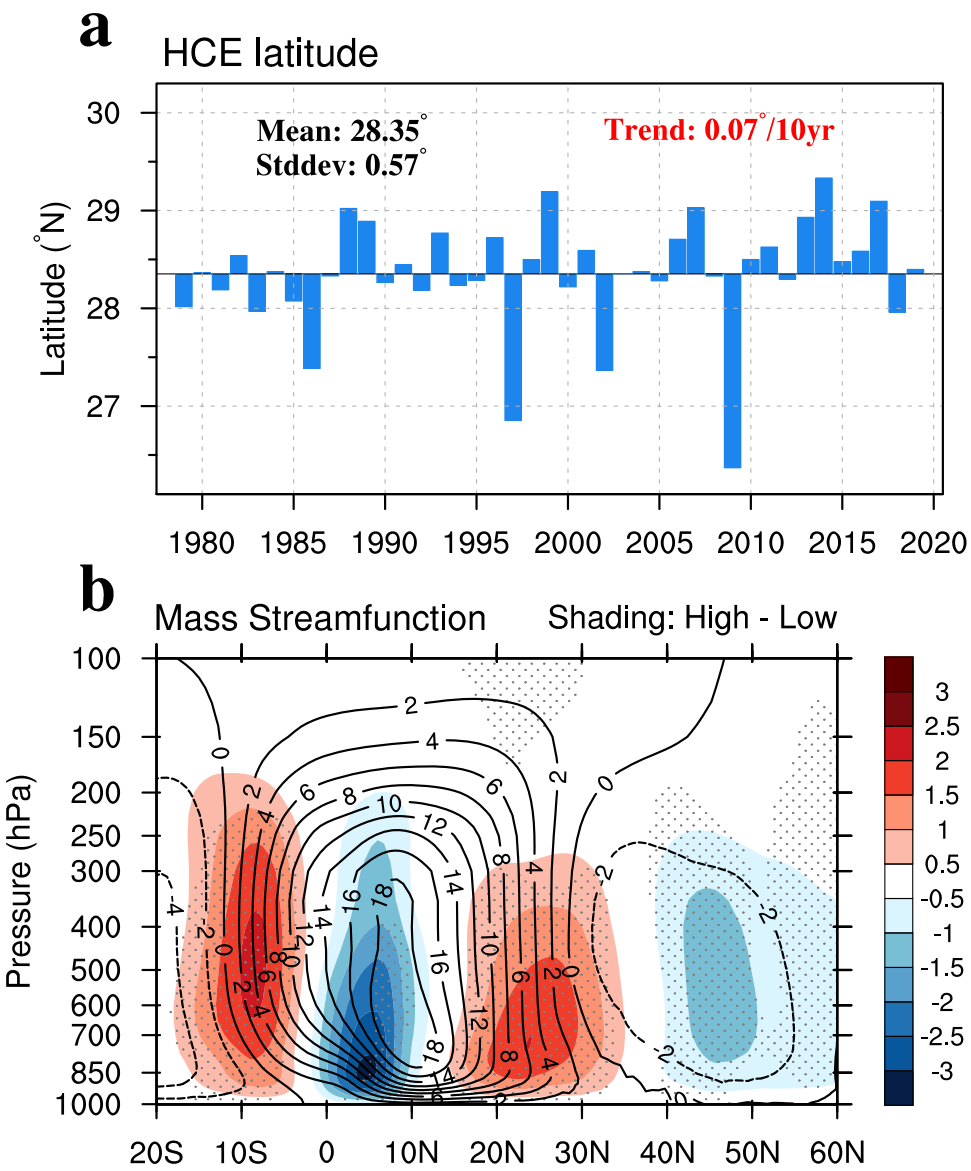

Fig. 1 Time series of HCE latitude and spatial structure of Hadley cell expansion. a Time series of the DJFM-mean HCE latitude (°N) for the period 1979 to 2019. **b** Mass streamfunction for climatology (contour) and high-minus-low HCE latitude year composite (shading) for DJFM. Units are 10^{10} kg s^{-1}. Stippling denotes a significant area at the 95% confidence level.

for high-minus-low HCE latitude composite. As seen in the vicinity of 30°–40°N, the anomalous EMFD from transient waves is significantly greater than that from stationary waves, and it is situated at and slightly north of a climatological zero-crossing (Fig. 3c), which pulls the HCE more poleward. A map of the EMFD field at 250 hPa (not shown) reveals several positive local peaks over the exit region of the Asia–Pacific jet, extending eastward over North America and near the Mediterranean; the multiple maxima in anomalous EP flux convergence between 20°N and 40°N shaded in Fig. 3b likely correspond to these separate jet exit regions. These regions correspond to major storm tracks[51,52], indicating once again the importance of transient eddies in HC expansion. Detailed regional analysis is left for future work.

These diagnostic findings corroborate the hypotheses proposed by Held[20], Korty, and Schneider[22], and Levine and Schneider[24]; when transient eddies from the midlatitudes enter the subtropics, they disrupt the angular momentum conserving flow, thereby slowing down the flow aloft, decreasing the vertical wind shear, and reducing the baroclinic instability. In this manner, the eddies act to expand the HC. The importance of changes in vertical shear (as opposed to changes in vertical static stability) and the order of events in shifting the HCE are explored more in the following section.

Transient waves and changes in baroclinicity

How, precisely, do the transient waves modify the subtropical baroclinicity, and hence HC expansion? To address this question, we compute the baroclinicity and EMF spectrum of the transient waves. Enhancement of the EMFD in the subtropics is anticipated to reduce the zonal-mean zonal wind and thus baroclinicity, which in turn creates a room for the HC to expand toward the pole. Although the main analyses are based on the zonal-mean dynamics, the investigation of the zonally varying Phillips[53] baroclinic instability criterion (BIC) yields additional, valuable insight (see Fig. 4a). This is calculated as:

$$\mathrm{BIC} = \frac{f^2(u_{250} - u_{850})}{\beta g H(\theta_{250} - \theta_{850})/\Theta_0}. \quad (2)$$

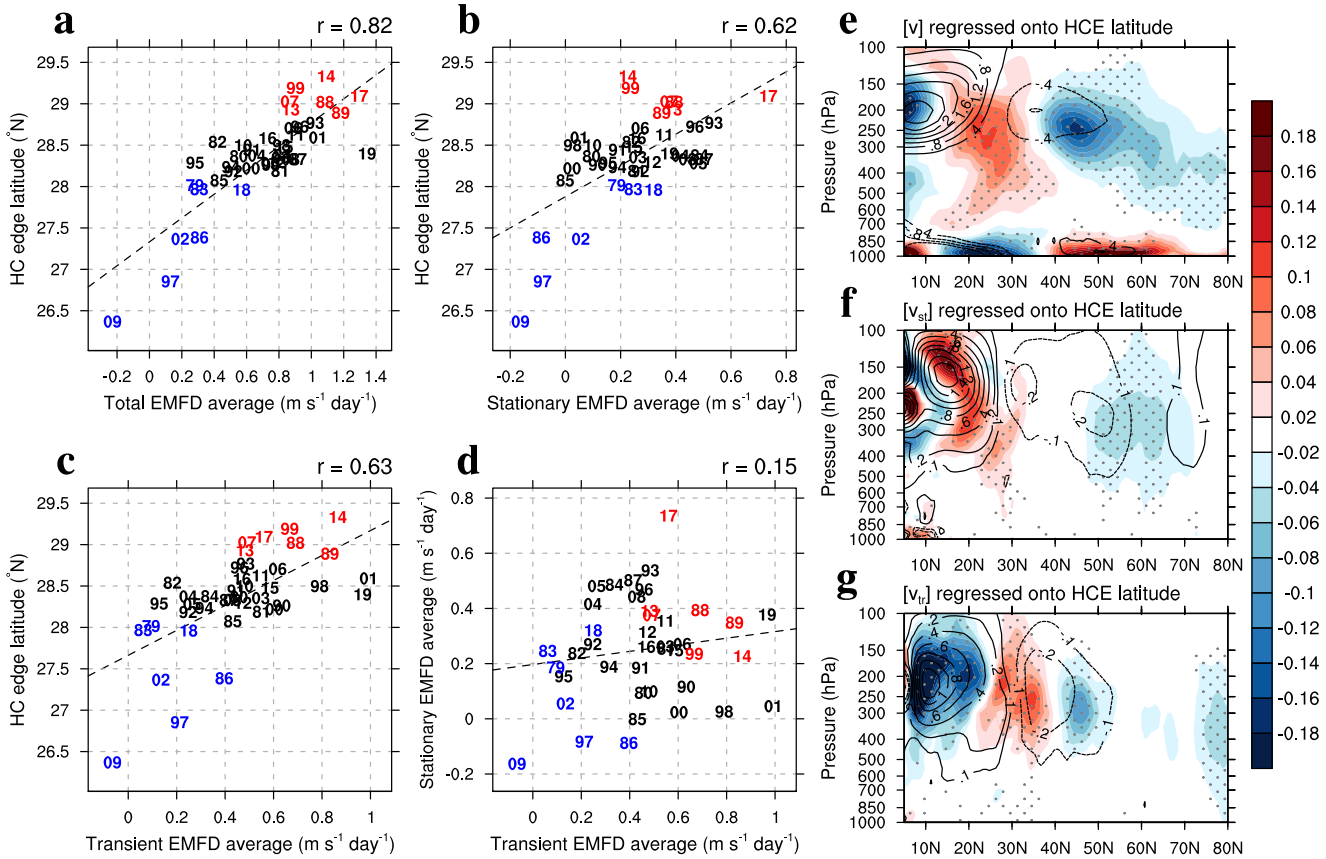

Fig. 2 Relationship between HCE latitude and stationary and transient waves. a Scatter plot of **a** HCE latitude vs. EMFD averaged over a box enclosed by [400–200 hPa, 20°–35°N] for individual years. The same as **a** except for **b** stationary wave, and **c** transient wave. **d** EMFD from stationary wave vs. that from the transient wave. The linear correlation is shown in the legend, and regression lines are superimposed. **e** Actual meridional winds (shading) regressed onto the HCE latitude time series shown in Fig. 1a, and the derived meridional winds (shading) from the **f** stationary and **g** transient EMFD forcing using Eq. (1), which are then regressed onto the HCE latitude time series. The contours in **e**–**f** represent the corresponding DJFM climatology and units for both the climatology and anomaly, which are m s^{-1}. Stippling indicates a significant area at the 95% confidence level.

Here, the vertical wind shear and potential temperature difference are measured between 250 and 850 hPa, H is the thickness of the air column between 250 and 850 hPa, β is $\frac{df}{dy}$, g is gravity, θ is potential temperature, and Θ_0 is the standard potential temperature (set here 290 K). Calculating, with a ceiling of 500 hPa, rather than 250 hPa (not shown), produces the same conclusion. Given the dependence of the transient eddies on the baroclinicity, we expect the HC to expand or contract in the meridional direction, in response to variations in baroclinicity[20,22,24]. In the high-minus-low HCE latitude composite (Fig. 4a), the BIC decreases along the climatological HCE region, with the reduction being most pronounced over the North Pacific and North Atlantic. Along with this reduction near 30°N, a poleward displacement of the main baroclinicity region is observable. Climatologically, the baroclinic zone, which is characterized by a stronger meridional temperature gradient, forms along 40°–45°N over the western Pacific and 40°–55°N over North America and the North Atlantic. However, the high-minus-low HCE latitude year composite of the BIC (Fig. 4a) exhibits an increase to the north of the existing maximum. The baroclinic eddy activity is displaced northward so that the thermally-driven overturning circulation originating from the tropics can reach further north than the normal state, causing the HCE to shift northward[20,22,54].

The map of vertical wind shear (not shown, in-depth regional analysis is deferred to subsequent work) for high-minus-low HCE latitude composite also demonstrates a reduction of shear along the HCE region, with a substantially stronger reduction over the North Pacific, Central America, and the North Atlantic, and all the way through the Mediterranean. However, the static stability field shows a negligible change along the ~30°N latitude circle (not shown), in contrast to the change associated with the global warming-induced HC expansion[11]. The relationship between the HCE and the baroclinicity near the descending branch (i.e., 25°–40°N) over the 41-year period is examined in Fig. 4b–e. A significant negative correlation exists between the two variables ($r = -0.72$), lending support to the previous hypothesis that a greater baroclinicity acts to terminate the angular momentum conserving regime more equatorward and results in a more equatorward generation of the baroclinic eddies and a more equatorward HC terminus. The change in baroclinicity is mainly caused by the change in vertical wind shear (Fig. 4d, $r = 0.89$), not the change in static stability (Fig. 4c, $r = 0.08$). In other words, the decrease in baroclinicity near the HCE latitude is primarily attributable to the decrease in vertical wind shear, which is associated with the decrease in the near-surface meridional temperature gradient (Fig. 4e, $r = -0.58$) as a result of the thermal wind relationship.

The vertical wind shear serves as a controlling parameter in year-to-year HC expansion[55], in contrast to the forced response of baroclinicity to greenhouse gas concentration increase, which has been shown to depend strongly on changes in static stability[4,11,54]. Note that the variation of the subtropical tropopause height, which has been considered to scale with the meridional width of the HC in Held and Hou[19] and others, exhibits a nearly

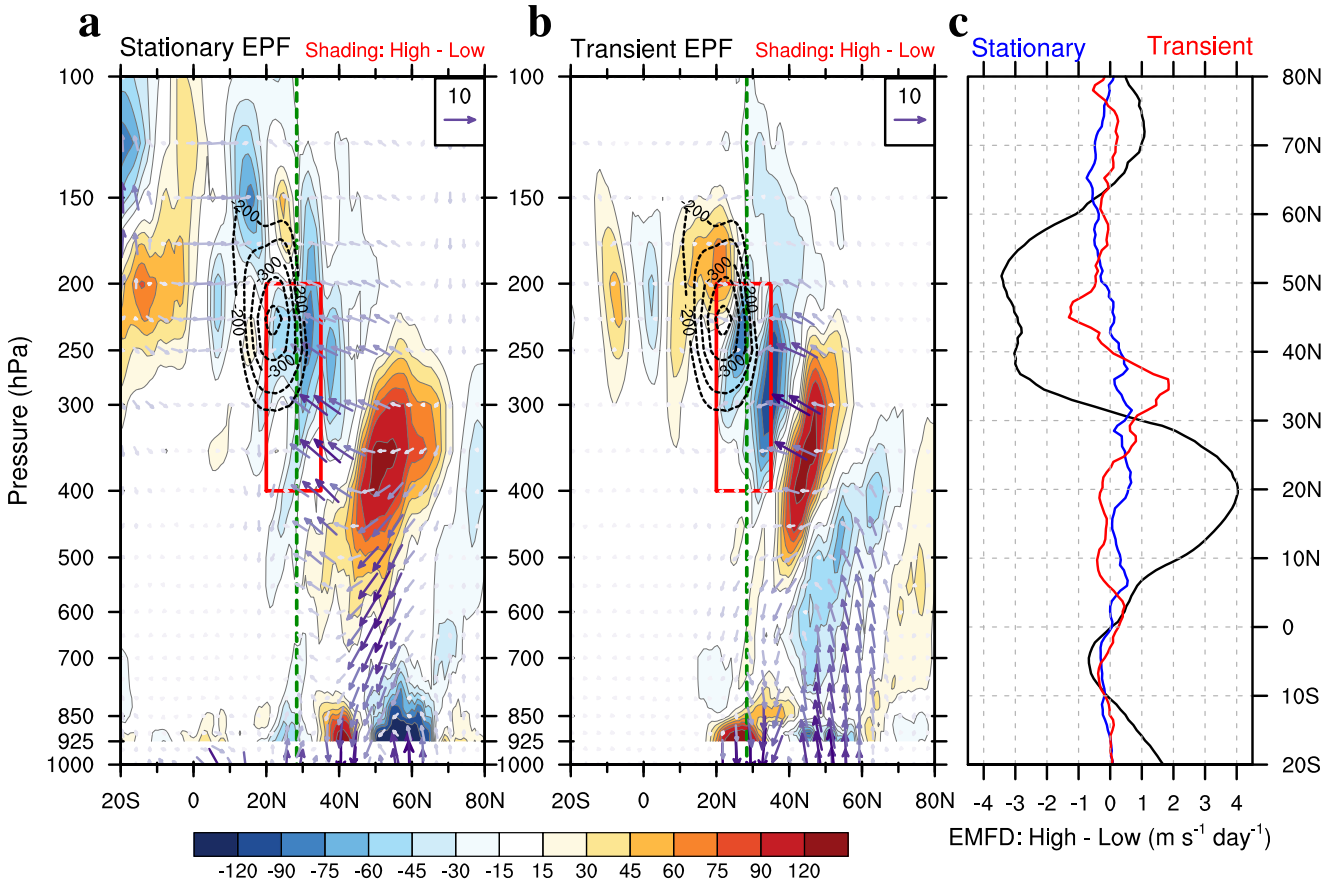

Fig. 3 Wave propagation and Hadley cell expansion. Eliassen–Palm flux (vector) and its divergence (shading, $m^2\,s^{-2}$) for **a** stationary and **b** transient waves for high-minus-low HCE latitude years. Climatological total EP flux convergence is overlaid with the thick dotted line with the outer contour denoting $-200\,m^2\,s^{-2}$. Green vertical dotted line indicates the climatological location of the HCE. **c** Climatological total EMFD (black, $m\,s^{-1}\,day^{-1}$) and EMFD of stationary (blue) and transient (red) waves for high-minus-low HCE latitude years at 250 hPa. **a**, **b** shading represents a significant area at the 95% confidence level and the red box is used to plot Figs. 2 and 5. Vector is represented with a deeper shade of purple proportional to its magnitude.

zero correlation with that of HCE ($r = -0.07$). A slightly different measure of baroclinic instability, calculated using the Eady growth rate at 500 hPa (not shown), reveals patterns and statistics akin to those of the BIC.

In order to determine the ordering of the processes described above, and to suggest possible causality, we perform a lead–lag analysis. Figure 5a shows that vertical wind shear between 20°–35°N decreases between zero-to-one months before corresponding decreases in EMFD. That is, the weakened or strengthened subtropical jet may lead to the change in EMFD (which we demonstrate below to be due to the change in critical latitude). Changes in EMFD (Fig. 5b) occur concurrently with changes in BIC (baroclinicity) with a small but statistically significant tendency for EMFD to lead BIC rather than lag. This can be interpreted as equatorward propagation and convergence of eddies, a deceleration of zonal winds in the upper troposphere, and a subsequent decrease in baroclinicity. Figure 5c illustrates the existence of a zero-to-one-month lead between the BIC change and the HCE response. This lead–lag analysis supports our storyline for year-to-year variations in the HCE latitude: a decreased vertical wind shear/weakened subtropical jet → a poleward shift in EMFD → a poleward shift in baroclinicity → a poleward shift in HCE. Some of these processes follow others after about a month, while others are simultaneous (or follow within a given month of each other).

The poleward shift of baroclinic wave activity can be explained to some extent by theory of linear critical latitude[11,56–58]. To verify this, we calculate the co-spectrum of the EMFD as shown in Fig. 6. A systematic poleward shift of subtropical and midlatitude waves is evident for both fast and slow waves in the Northern and Southern Hemispheres (see red contours over [20°N, 40°N] and [30°S, 50°S]). As suggested by Menzel et al.[34], Robinson[59], and Seager et al.[60], the poleward expansion of EMFD at the poleward flank of the spectra can be attributed to the weakening of the thermally-driven subtropical jet during high HCE events (see the blue and red lines on the right side of Fig. 6), where the meridional temperature gradient tends to flatten, as is commonly observed during the cold phase of ENSO. To elaborate further, this weakening of the zonal wind over 10°–50°S or 10°–30°N shifts the critical latitudes poleward, thereby confining the wave activity to higher latitudes. This gives rise to a poleward shift in wave breaking and the anomalous EMFD. These features are consistent with the numerical modeling results of Lu et al.[11], which showed that the HC contracts (expands) during El Niño (La Niña) years. Since HCE is determined by the wave breaking within the downward branch of the HC (i.e., EMFD) due to the equatorward propagation of EP flux and its convergence toward the region of large positive refractive index, the linear critical latitude theory functions reasonably well for the interannual variability of the HCE.

Consistent with Fig. 4, the poleward shift of eddy source region (i.e., eddy momentum flux convergence) is observed from blue dotted contours in Fig. 6 (i.e., the dotted contours are positioned more poleward compared to the green shading over [30°, 60°N]). This shifts baroclinicity poleward, expanding the HC. Both in the NH and SH higher latitude regions (i.e., 40°–60°N, 50°–70°S), a

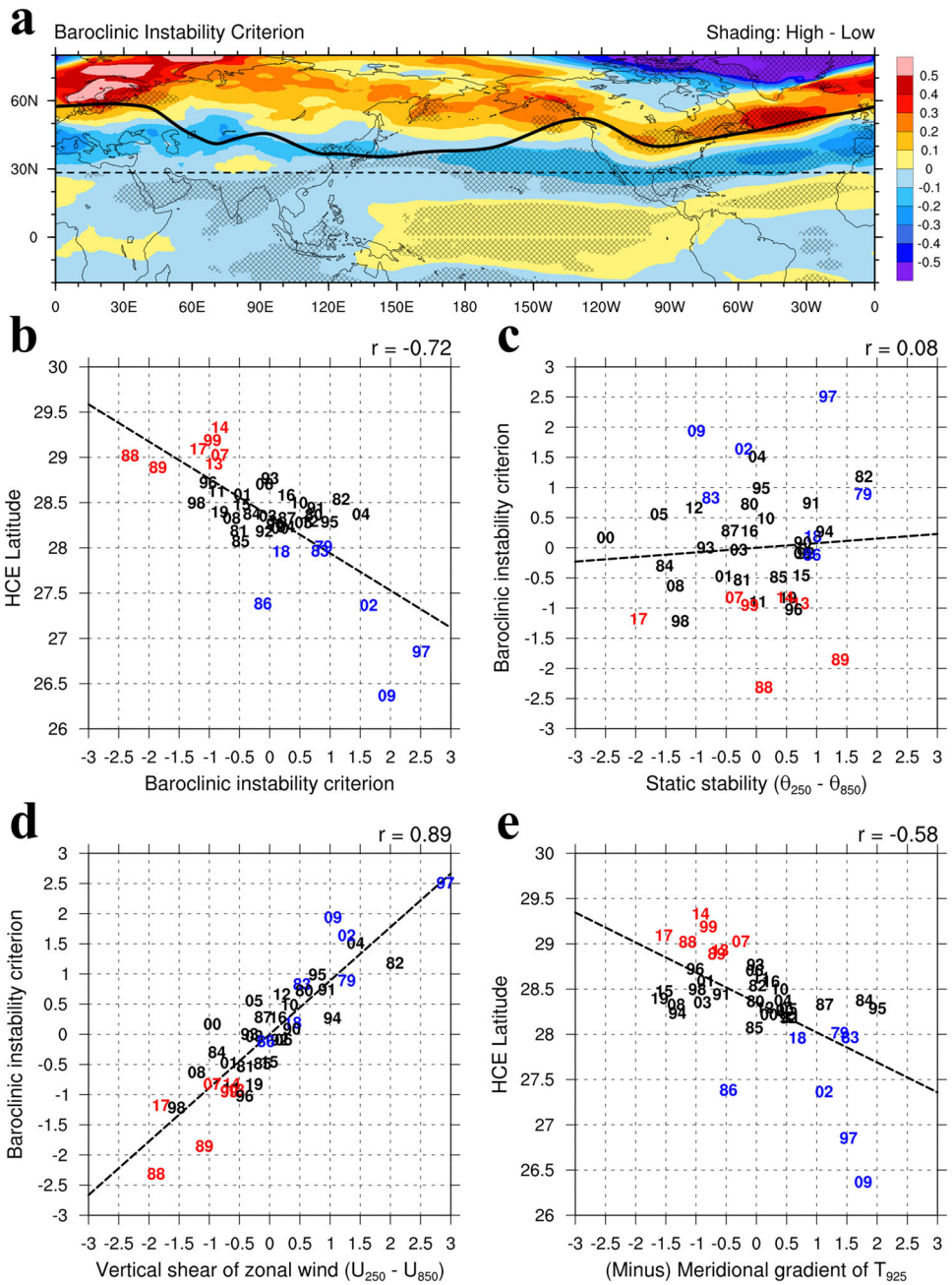

Fig. 4 Relationship between HCE latitude and baroclinicity. a Phillips (1954)' baroclinic instability criteria (BIC). Shading is a high-minus-low HCE latitude year composite, and the thick black curve roughly follows the climatological local maxima. The dotted horizontal line denotes the climatological HCE location. Stippling indicates a significant region at the 95% confidence level. **b** BIC vs. HCE latitude (°N), **c** bulk static stability (K) vs. BIC, **d** vertical wind shear (m s^{-1}) vs. BIC, and **e** (–)meridional temperature gradient at 925 hPa (K m^{-1}) vs. HCE latitude (°N) for the latitudinal domain [20°–35°N]. **b**–**e** all abscissae have been standardized.

poleward displacement of co-spectrum leads to the poleward shift of eddy-driven jet, characteristics that resemble those in response to global warming (see Fig. 10 in Lu et al.[11]).

Potential drivers of the HCE shift

What atmospheric or oceanic factors are associated with the HC expansion or contraction? To address this, we first examine the high-minus-low HCE latitude composite in the geopotential height (contours in Fig. 7a) and zonal wind (shading) fields at 500 hPa. Immediately apparent is the large positive geopotential anomaly over the North Pacific—which is part of the negative phase of the well-known Pacific–North America (PNA) teleconnection pattern—as well as a negative anomaly over Canada and a weaker positive anomaly over the southeastern United States. This negative PNA-like pattern is often associated with a La Niña-like SST forcing—note also La Niña-like cold tongue is even evident in Fig. 7b. Another notable feature is the pronounced negative geopotential height anomaly over Greenland and neighboring positive anomaly over the midlatitude Atlantic. Considering the quasi-barotropic nature of the circulation over the extratropics, this pattern, along with the anticyclonic circulation anomaly over the North Pacific, resembles the positive phase of the AO—note also the cold skin temperatures over Greenland and the warm temperatures over Eurasia. This is consistent with a finding by

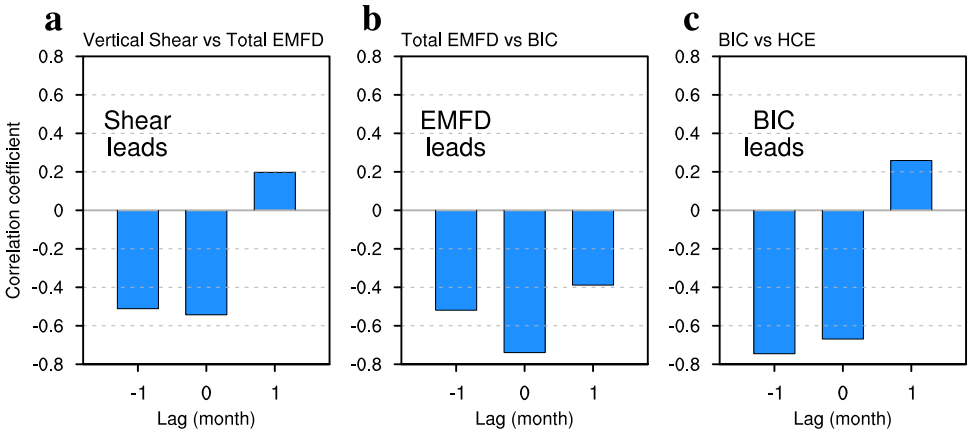

Fig. 5 Temporal correlation of related variables with HCE variation. Lead–lag correlation coefficients between **a** vertical shear vs EMFD, **b** EMFD vs BIC (baroclinicity), and **c** BIC vs HCE, using DJFM monthly data. The averaged latitudinal domain is [20°–35°N].

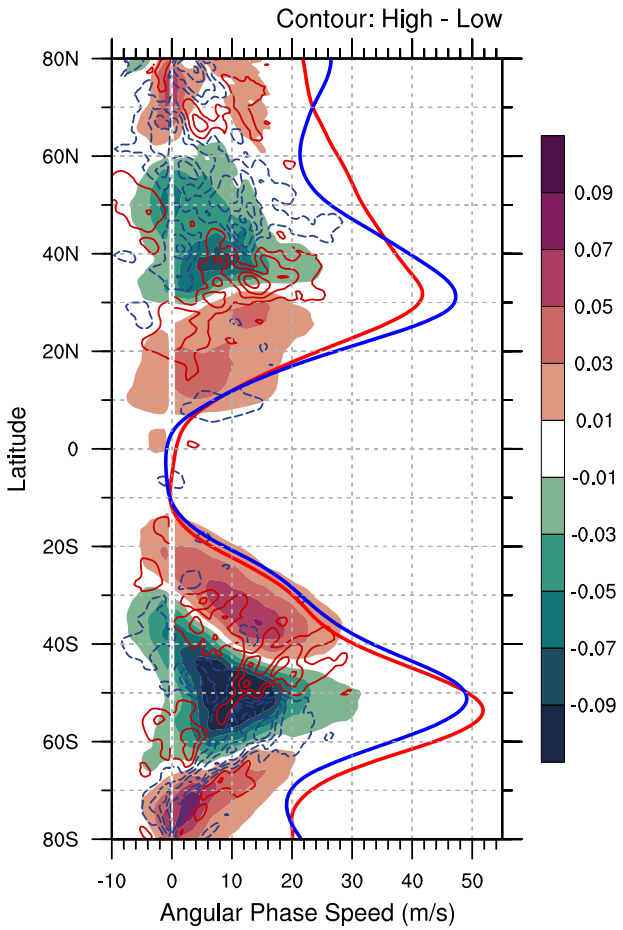

Fig. 6 Spectral analysis and application of critical latitude theory. Co-spectrum (m s^{-1} day^{-1}) of the EMFD at 250 hPa (red and blue contour, intervals of 0.02 m s^{-1} day^{-1} with zero omitted) during DJFM for high-minus-low HCE latitude years with climatology (shading, intervals of 0.02 m s^{-1} day^{-1}). On the right side are the 250-hPa zonal winds (m s^{-1}) divided by *cos*(latitude) for high (red line) and low (blue) HCE years.

Hu et al.[35], which states that a positive phase of the AO results in a poleward displacement of the HCE via the EMF mechanism.

The results shown in Fig. 7a, b suggest that El Niño/La Niña and AO variabilities are the most influential internal causes of interannual HC expansion/contraction. To further verify this, the sign and magnitude of the HCE latitude anomalies are plotted in terms of the color and size of the filled circles in the space spanned by the índices of AO and NIÑO3.4 (Fig. 8a). Here, we can see the negative relationship with a slope connecting the second quadrant to the fourth quadrant via the origin. Greater HC expansion is associated with a negative NIÑO3.4 index and a positive AO index, and vice versa for contraction, despite the presence of a few large red patches along the $y = x$ line. The linear correlation of HCE latitudinal variation with NIÑO3.4 index and with AO index are −0.48 and 0.55, respectively. Nearly zero correlation exists between the AO and NIÑO3.4 indices ($r = -0.01$).

To see the HCE response to these modes, the meridional winds are regressed against the time series of the −NIÑO3.4 and AO indices over the 41-year period (Fig. 8b, c). Given the dearth of correlation between the two indices, it is perhaps not surprising that the wind anomalies in the two plots are quite dissimilar. In Fig. 8b (−NIÑO3.4 regression), significant positive area is seen in the free troposphere centered around [28°N, 400 hPa] and extending to 35°N, whereas in Fig. 8c (AO regression), positive area is observed at higher levels over the 20°–40°N latitude band. These two indices can serve as independent predictors for the HCE latitude and the resulting linear multiple regression model using these two predictors is as follows:

$$\text{Latitude of HCE } (^{\circ}\text{N}) = -0.27 \times \text{NIÑO3.4} + 0.31 \times \text{AO} + 28.35. \quad (3)$$

This regression model explains ~60% of the total variance in interannual HCE variation with a prediction skill of 0.73. Equation (3) implies that the two internal oscillations contribute nearly equally to the variation in HCE, which is consistent with the similar correlations between each predictor and the predictand. However, the moderate amount of the total variance implies the possibility that other processes may be important.

We have shown that the interannual variation of HCE latitude is largely associated with ENSO variability[32,45] and extratropical variability such as AO. While ENSO is considered an efficient driver for the HCE shift based on a set of model simulations[11], the AO as a driver still needs to be verified through a sensitivity test. The positive AO signifies the poleward shift in baroclinicity, which alone—in the absence of wave breaking—could induce the HC expansion. However, an examination of the change in zonal wind according to the AO phase (Fig. 9) reveals a more intricate storyline; when the AO is in its positive phase, the polar jet stream intensifies (more so than in the HCE composite case shown in Fig. 6) and moves poleward. This shift is accompanied by a weakening of the subtropical jet near the HC edge[61], causing the equatorward propagating EP flux to converge further poleward

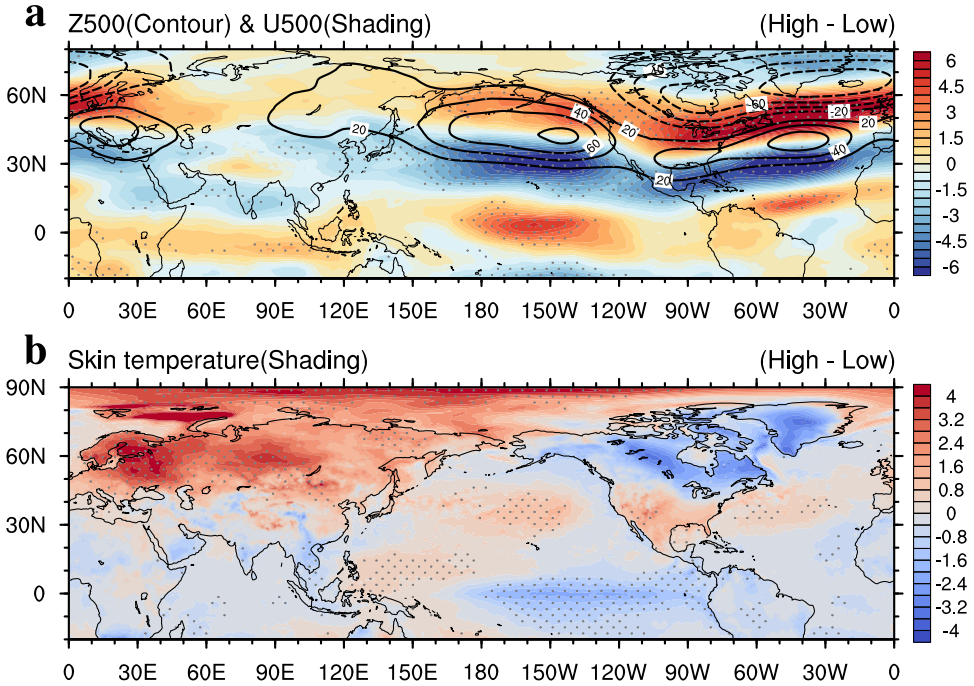

Fig. 7 Horizontal distribution of upper-level geopotential and surface temperature at the peak of expansion. Composites of **a** geopotential height (contour, m) and zonal wind (shading, m s^{-1}) at 500 hPa and **b** skin temperature (K) for high-minus-low HCE latitude years. Stippling indicates a significant region at the 95% confidence level.

(at 30°–40°N, instead of 8°–32°N as in Fig. 3a; this is not shown, though it can be inferred from Fig. 6)[35]; HC expansion follows. Though the subtropical jet weakens primarily over the Pacific sector during the positive AO phase[61], the exact reason for this weakening requires further investigation.

The dynamical pathways responsible for the poleward shift of the HCE, which are not mutually exclusive, can be summed up as follows (cf, the equatorward shift of the HCE also holds, but with the signs of each respective anomaly or shift reversed):

Pathway 1) weakened thermal driving from the tropics → decreased vertical wind shear / weakened subtropical jet → poleward shift in critical latitude → poleward shift in EMFD, poleward shift in baroclinicity → poleward shift in HC edge;

Pathway 2) poleward shift in eddy source region → poleward shift in baroclinicity → poleward shift in HC edge;

Pathway 3) mixture of (1) and (2): poleward shift in eddy source region and/or polar jet) → weakened subtropical jet → poleward shift in critical latitude → poleward shift in EMFD, poleward shift in baroclinicity → poleward shift in HC edge.

Note here that the connected processes are tightly coupled so that these can also respond instantaneously with each other.

Figure 10 schematically depicts the aforementioned physical processes regulating the interannual latitudinal variation of the HCE. Here, the EP flux (or negative EMF) representing wave activity propagation caused by both stationary and transient eddies is plotted to illustrate the role in the poleward expansion of the HC. The greater contribution of the transient wave to the shifting of the HCE toward the pole is also highlighted. Two interannually dominant modes of natural variability (El Niño/La Niña and AO) are also displayed in the tropics and extratropics.

NH summer HCE shift

The variation in NH summer (June–July–August–September, JJAS) HCE is also examined in Supplementary Figs. 2–7. Although the JJAS NH HC is significantly weakened and the average edge is located further north than the winter counterpart, the gross features are nearly identical. Compared to the winter case, the subtropical jet is marginally weaker and more poleward in the summer.

The correlation between the NIÑO3.4 (or AO) index and the HCE latitudinal variation during the boreal summer is only –0.35 (0.32, respectively). Using the aforementioned two variables to construct the regression equation (Supplementary Fig. 7) yields a correlation coefficient of 0.44, which is also lower than its counterpart for the boreal winter. This is unsurprising, as ENSO and its teleconnections are strongest during boreal winter.

Verification of statistical characteristics by using CMIP5 simulations

The proposed statistical processes for HCE change are verified using historical simulation data from twenty-eight CMIP5 models (Supplementary Fig. 8). The key insight from the aforementioned observational analysis is the dependence of interannual HCE latitudinal variation on the change in baroclinicity. Therefore, for each model, HCE latitude is plotted against the BIC using 250 and 850 hPa zonal winds for each year (DJFM), and their correlation is calculated (Supplementary Fig. 8). The observed negative linear relationship is captured in all models (with an average of –0.55), albeit with a reasonable amount of variation. Out of these 28 models, 12 models that have an absolute correlation value greater than 0.60 are selected for high correlation group (HIGH), whereas 9 models with the absolute value less than 0.50 is chosen for low correlation group (LOW). The average correlations for the selected high correlation and low correlation model groups are –0.69 and –0.38, respectively. The respective standard deviations are 0.05 and 0.09, indicating a lower spread in the HIGH group.

As shown in Supplementary Fig. 9, EMFDs for total, stationary, and transient waves are highly correlated with the HCE latitudinal variation for the HIGH group, whereas the LOW group shows weaker correlations. The similar results are found for the NIÑO3.4 and AO indices: significantly higher correlations of El Nino/La Nina and AO with HCE latitudinal change in the HIGH group. The combined natural variability ((–) NIÑO3.4 + AO) reveals an even greater disparity in the prediction skill of the two groups. Average

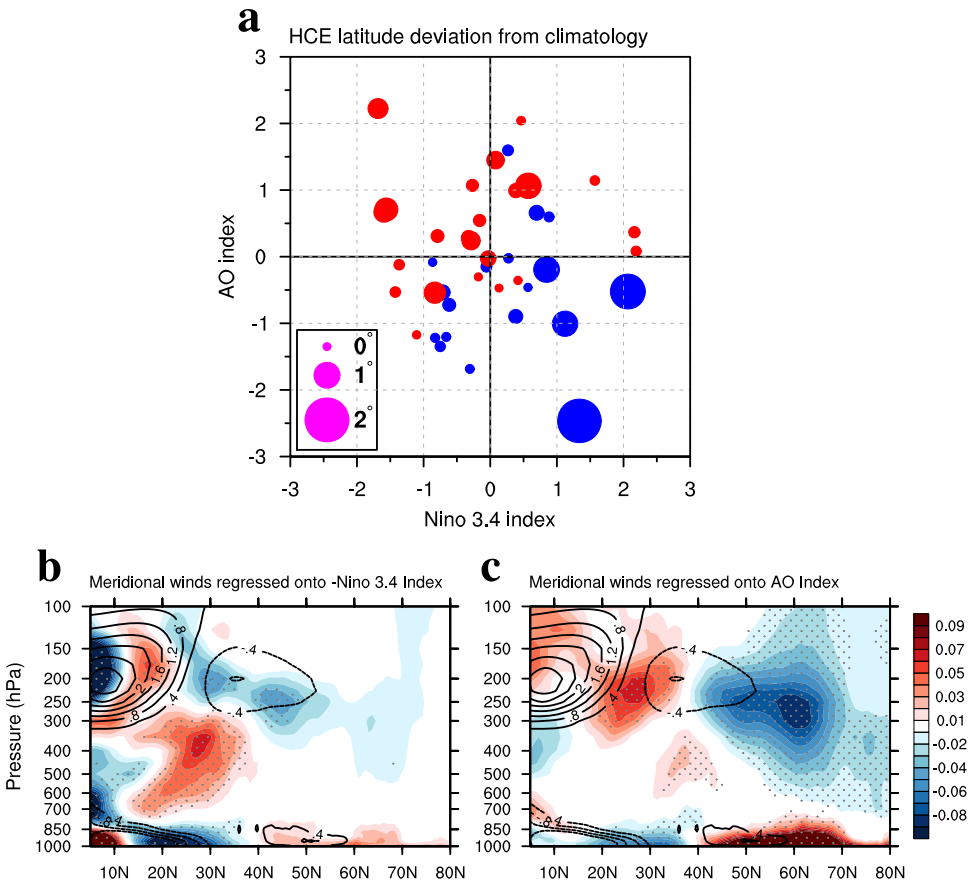

Fig. 8 HCE latitude as a function of two natural variabilities. a Scatter plot of HCE latitude deviation from mean (using Fig. 1a) with respect to the axes of NIÑO3.4 and AO indices for 41-year data. Positive (negative) deviations are shown as the red (blue) dots with their size representing the magnitude of HCE latitude deviation. Meridional winds (m s^{-1}) regressed against **b** –NIÑO3.4 and **c** AO index time series. **b**, **c** contour is climatological meridional wind and stippling indicates a significant region at the 95% confidence level.

correlations presented for two groups are all statistically distinct at the 95% confidence level. All of these imply the importance of EMFD (particularly that by transient waves) and the related natural variability of the ENSO and AO in the interannual variation of the HCE latitudinal shift, which align with findings from the reanalysis data. Nevertheless, since the current CMIP5 results do not directly support the dynamical mechanisms, a more thorough future analysis is warranted.

DISCUSSION

The HC expands or contracts on an interannual time scale; however, its underlying causes are poorly understood[5]. The HC's poleward expansion poses a significant hazard to a significant portion of the world's population via increases in the frequency of drought, forest dieback, and fire. Using the ERA5 and CMIP5 data, this study investigates the physical mechanisms of the interannual variation in the HCE in the NH and presents a related statistical prediction model.

The HCE is determined by EMF activity from both stationary and transient waves. Using the momentum equation, we showed that EMFD of transient waves plays a larger role than that of stationary waves in determining the meridional wind—though both are significant. Furthermore, transient waves drive the HCE further poleward than stationary waves do. This greater significance of transient waves is the result of a reduction in baroclinicity near 30°N (which is predominantly attributable to a reduction in vertical wind shear) and a poleward shift of the main baroclinic zone[62]. The variation in HC width on the interannual time scale can be contrasted to the expansion under the influence of anthropogenic warming, with increased subtropical static stability postulated as the primary cause of the expansion for the latter[11,54]. The interannual shifts of the HCE are consistent with the linear critical latitude theory, in which the poleward shift of the HCE is associated with a weakening of the background wind speed over the subtropics.

In addition, the interannual variation of the HCE latitude is found to be related to two natural modes of variability: ENSO, the leading mode of atmosphere–ocean coupled variability in the tropics, and the AO, the leading mode of extratropical atmospheric internal variability. These two modes contribute about equally and their sum accounts for 60% of the total interannual variation of the HCE by modulating the propagation of stationary and transient waves.

To verify some of the observed results, twenty-eight CMIP5 simulations are analyzed, which demonstrates that models with higher interannual correlations (>0.6) between the HCE and BIC exhibit ~50% higher correlations between the HCE variation and EMFD time series. Even the greater differences are found in the relationships of HCE with NIÑO3.4 and AO indices between high and low correlation model groups. These statistical characteristics are similar to those observed.

The stratospheric variability and factors, including the Quasi-Biennial Oscillation[63], tropical lower-stratospheric temperature warming[64], and water vapor in the lowermost stratosphere over the Arctic[65], have been suggested to affect the HCE. These are evaluated at the interannual time scale. The calculated

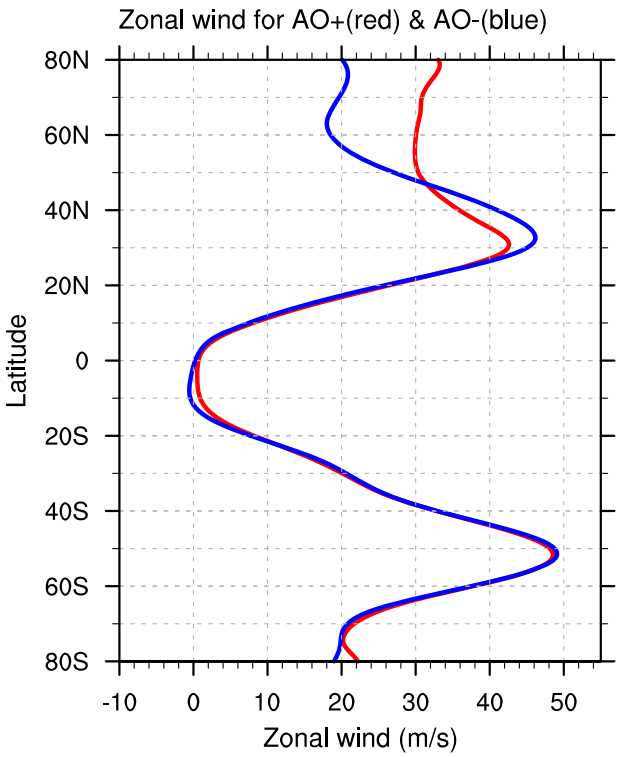

Fig. 9 Zonal winds for AO phase. 250-hPa zonal winds ($m\,s^{-1}$) divided by *cos*(latitude) for the positive (red line) and negative (blue) AO phases. The AO index greater (less) than 1.0 (–1.0) is used for the positive (negative) phase.

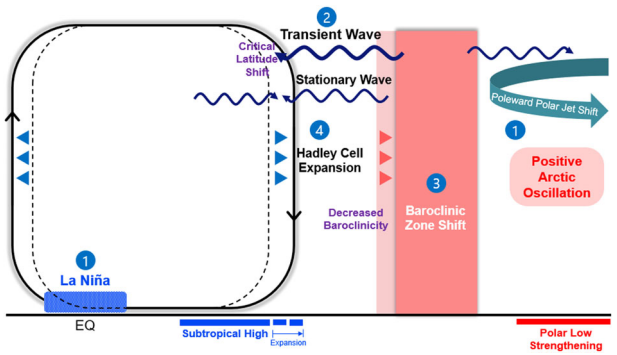

Fig. 10 Postulated physical processes. Schematic showing the main physical processes for controlling the HCE latitudinal variation on the interannual time scale. The temporal sequences are denoted as the numbers with a filled circle. La Niña and the positive phase of the AO are the main tropical and extratropical forcing sources for the Hadley cell expansion. Wave activity propagation from both stationary and transient waves is plotted as meridionally directed arrows. The reduction in subtropical baroclinicity and the resulting poleward shift in the baroclinic zone are presented. The poleward expansion of subtropical high is also indicated. Poleward polar jet stream and strengthened polar low are observed at the positive AO phase.

correlations for these factors are all below 0.25, indicating no significant relationship with the stratospheric variations.

Note that in a future warming climate, widening is anticipated during boreal winter[6,8,30], and a statistically significant trend in width variation should emerge by the end of 21st century, when the variation from external forcing of anthropogenic sources exceeds the internal climate variation in the HCE latitude. Since both atmosphere–ocean coupled variability and internal atmospheric variability are greatest during the NH winter season, the precise timing of this conversion to the signal is highly model dependent and uncertain, as stated in Staten et al.[5]. In contrast, summer and fall HCE is more susceptible to external forcing, and a significant linear trend has already been detected during the satellite era[7].

The following questions can be explored in future work: how do the widening/contraction mechanisms for the austral winter and spring HCE compare to those of the NH? A preliminary hypothesis suggests that a more zonally symmetric configuration in the SH produces fewer stationary waves; consequently, an even greater contribution from transient waves in the SH is anticipated. In addition, the Southern Annular Mode or Antarctic Oscillation[36] activity is expected to be the primary factor modulating the interannual HCE latitudinal variation. The ENSO fluctuations during the austral winter are more mild than in boreal winter, which will also diminish the influence of stationary waves. A more quantitative evaluation of these and additional factors will be conducted in the future. A comprehensive understanding of the entire process related to the HC, including HCE, at the interannual time scale, may necessitate considering the characteristics shaped by the tropical convective source from longitudinally varying preferred regions[1,66], as well as the dynamics of the eddy-driven jet.

METHODS

Observations

To identify the mechanisms of interannual variation of the HCE, we examine the NH extended winter (DJFM) and summer (JJAS) seasons. Six hourly or monthly ERA5 data[67], including zonal (u) and meridional winds (v), temperature, and geopotential height, for the period from 1979 to 2019 (41 years), are utilized. These data consist of 37 vertical levels ranging from 1000 hPa to 1 hPa and are used to calculate atmospheric variables such as the mass streamfunction, EMF, and eddy heat flux. The interannually varying AO index was derived from the seasonal mean sea-level pressure. HadISST[68] is employed to compute the NIÑO3.4 sea surface temperature (SST) index for the same time period since HadISST is based primarily on observational data so that it can be used for a more direct representation of SST variations.

Calculations of HCE location, EMF, and co-spectrum

To calculate the HCE, the zonally averaged mass streamfunction (ψ) is computed by integrating the density-weighted zonal-mean meridional wind from the top of the atmosphere downward to 1000 hPa: $\psi = -\frac{1}{g}\int 2\pi a\cos\varphi[\overline{v}]dp$, where g is gravitational acceleration, φ is latitude, v denotes meridional wind, and p is pressure. The overbar and square brackets indicate time and zonal means, respectively. The HCE latitude is then determined based on the first zero-crossing latitude of this streamfunction at 500 hPa as one moves poleward from the peak of the streamfunction[5,42–44].

EMF ($[u^*v^*]$) is calculated by deriving the zonal deviations of the 6-hourly u and v from their respective zonal means at each grid point, multiplying them together, and taking the seasonal mean. The stationary EMF ($[\overline{u}^*\overline{v}^*]$) is derived by taking the zonal deviations from the monthly averaged u and v and calculating the seasonal average after multiplying two quantities. The transient EMF ($[\overline{u'^*v'^*}]$) is computed by taking the zonal deviations after obtaining the 6-hourly deviations (denoted as prime) of u and v from their monthly means, multiplying those two quantities, and calculating the seasonal mean.

The latitude–phase-speed spectrum of the EMFD is utilized to characterize the meridional propagation of baroclinic eddies[11,56,57,69]. Using space–time spectral analysis[70], the EMFD is decomposed as a function of the zonal wavenumber and frequency. In accordance with Randel and Held[56] and Chen and

Held[57], the co-spectrum is then transformed into the space of zonal wavenumber and angular phase speed. Finally, the EMFD spectrum is summed over wavenumber at each latitude, resulting in a spectrum density as a function of latitude and angular phase speed. As in Chen and Held[57] and Lu et al.[11], the co-spectrum is illustrated by multiplying the angular phase speed by the Earth's radius.

High and low HCE latitude years and composites

The seven most poleward HCE cases (i.e., high HCE latitude years: 1988, 1989, 1999, 2007, 2013, 2014, and 2017) and seven most equatorward HCE cases (i.e., low HCE latitude years: 1979, 1983, 1986, 1997, 2002, 2009, and 2018) are selected from the 41-year reanalysis dataset. This represents the highest or lowest ~17% of all years. The Student's *t* test is used to determine statistical significance at the 95% confidence level.

DATA AVAILABILITY

Six hourly and monthly ERA5 data (https://www.ecmwf.int/en/forecasts/datasets/reanalysis-datasets/era5)[67] can be freely obtained through the internet. The data and code used during the study are available upon request. Please contact the corresponding author at khseo@pusan.ac.kr. To validate the proposed mechanisms, twenty-eight CMIP5 historical run outputs[71] from 1950 to 2004 are used. The analyzed data are monthly data, and the datasets are interpolated into a $2.5° \times 2.5°$ longitude–latitude grid to facilitate comparisons. The 28 models are as follows: ACCESS1-0, ACCESS1-3, BCC-CSM1-1, BCC-CSM1-1-m, BNU-ESM, CanESM2, CCSM4, CMCC-CESM, CMCC-CM, CMCC-CMS, CNRM-CM5, CSIRO-Mk3-6-0, FGOALS-g2, GFDL-CM3, GFDL-ESM2G, GFDL-ESM2M, IPSL-CM5A-LR, IPSL-CM5A-MR, IPSL-CM5B-LR, MIROC5, MIROC-ESM, MIROC-ESM-CHEM, MPI-ESM-LR, MPI-ESM-MR, MPI-ESM-P, MRI-CGCM3, MRI-ESM1, and NorESM1-M.

CODE AVAILABILITY

The codes used in this study are available on request from the corresponding authors.

Received: 13 June 2023; Accepted: 23 November 2023;
Published online: 07 December 2023

REFERENCES

1. Hoskins, B. J., Yang, G.-Y. & Fonseca, R. The detailed dynamics of the June–August Hadley cell. *Q. J. R. Meteorol. Soc.* **146**, 557–575 (2020).
2. Davis, S. M. & Rosenlof, K. H. A multidiagnostic intercomparison of tropical-width time series using reanalyses and satellite observations. *J. Clim.* **25**, 1061–1078 (2012).
3. Lucas, C., Timbal, B. & Nguyen, H. The expanding tropics: a critical assessment of the observational and modeling studies. *Wiley Interdiscip. Rev. Clim. Chang.* **5**, 89–112 (2014).
4. Son, S.-W., Kim, S.-Y. & Min, S.-K. Widening of the Hadley cell from last glacial maximum to future climate. *J. Clim.* **31**, 267–281 (2018).
5. Staten, P. W., Lu, J., Grise, K. M., Davis, S. M. & Birner, T. Re-examining tropical expansion. *Nat. Clim. Chang.* **8**, 768–775 (2018).
6. Xian, T. et al. Is Hadley cell expanding? *Atmosphere* **12**, 1699 (2021).
7. Hu, Y., Huang, H. & Zhou, C. Widening and weakening of the Hadley circulation under global warming. *Sci. Bull.* **63**, 640–644 (2018).
8. Xia, Y., Hu, Y. & Liu, J. Comparison of trends in the Hadley circulation between CMIP6 and CMIP5. *Sci. Bull.* **65**, 1667–1674 (2020).
9. Vallis, G. K., Zurita-Gotor, P., Cairns, C. & Kidston, J. Response of the large-scale structure of the atmosphere to global warming. *Q. J. R. Meteorol. Soc.* **141**, 1479–1501 (2015).
10. Grise, K. M. et al. Recent tropical expansion: natural variability or forced response? *J. Clim.* **32**, 1551–1571 (2019).
11. Lu, J., Chen, G. & Frierson, D. M. W. Response of the zonal mean atmospheric circulation to El Niño versus global warming. *J. Clim.* **21**, 5835–5851 (2008).
12. Cayan, D. R. et al. Future dryness in the southwest US and the hydrology of the early 21st century drought. *Proc. Natl Acad. Sci. USA* **107**, 21271–21276 (2010).
13. Hoerling, M. et al. On the increased frequency of Mediterranean drought. *J. Clim.* **25**, 2146–2161 (2012).
14. Cai, W. & Cowan, T. Southeast Australia autumn rainfall reduction: a climate-change-induced poleward shift of ocean–atmosphere circulation. *J. Clim.* **26**, 189–205 (2013).
15. Post, D. A. et al. Decrease in southeastern Australian water availability linked to ongoing Hadley cell expansion. *Earth's Future* **2**, 231–238 (2014).
16. Fu, R. et al. Increased dry-season length over southern Amazonia in recent decades and its implication for future climate projection. *Proc. Natl Acad. Sci. USA* **110**, 18110–18115 (2013).
17. Studholme, J. & Gulev, S. Concurrent changes to Hadley circulation and the meridional distribution of tropical cyclones. *J. Clim.* **31**, 4367–4389 (2018).
18. Seo, K.-H., Frierson, D. M. W. & Son, J.-H. A mechanism for future changes in Hadley circulation strength in CMIP5 climate change simulations. *Geophys. Res. Lett.* **41**, 5251–5258 (2014).
19. Held, I. M. & Hou, A. Y. Nonlinear axially symmetric circulations in a nearly inviscid atmosphere. *J. Atmos. Sci.* **37**, 515–533 (1980).
20. Held, I. M. The general circulation of the atmosphere. 2000 WHOI GFD Program, Woods Hole Oceanographic Institution, Woods Hole, MA, https://gfd.whoi.edu/gfd-publications/gfd-proceedings-volumes/2000-2. 54 (2000).
21. Frierson, D. M. W., Lu, J. & Chen, G. Width of the Hadley cell in simple and comprehensive general circulation models. *Geophys. Res. Lett.* **34**, L18804 (2007).
22. Korty, R. L. & Schneider, T. Extent of Hadley circulations in dry atmospheres. *Geophys. Res. Lett.* **35**, L23803 (2008).
23. Homeyer, C. R. & Bowman, K. P. Rossby wave breaking and transport between the tropics and extratropics above the subtropical jet. *J. Atmos. Sci.* **70**, 607–626 (2013).
24. Levine, X. J. & Schneider, T. Baroclinic eddies and the extent of the Hadley circulation: an idealized GCM study. *J. Atmos. Sci.* **72**, 2744–2761 (2015).
25. Son, S.-W. et al. Impact of stratospheric ozone on southern hemisphere circulation change: a multimodel assessment. *J. Geophys. Res. Atmos.* **115**, D00M07 (2010).
26. Kang, S. M., Polvani, L., Fyfe, J. & Sigmond, M. Impact of polar ozone depletion on subtropical precipitation. *Science* **332**, 951–954 (2011).
27. Polvani, L. M., Waugh, D. W., Correa, G. J. P. & Son, S.-W. Stratospheric ozone depletion: The main driver of twentieth-century atmospheric circulation changes in the southern hemisphere. *J. Clim.* **24**, 795–812 (2011).
28. Allen, R. J., Sherwood, S. C., Norris, J. R. & Zender, C. S. Recent northern hemisphere tropical expansion primarily driven by black carbon and tropospheric ozone. *Nature* **485**, 350–354 (2012).
29. Tao, L., Hu, Y. & Liu, J. Anthropogenic forcing on the Hadley circulation in CMIP5 simulations. *Clim. Dyn.* **46**, 3337–3350 (2016).
30. Grise, K. M. & Davis, S. M. Hadley cell expansion in CMIP6 models. *Atmos. Chem. Phys.* **20**, 5249–5268 (2020).
31. Mitas, C. M. & Clement, A. Has the Hadley cell been strengthening in recent decades? *Geophys. Res. Lett.* **32**, L03809 (2005).
32. Amaya, D. J., Siler, N., Xie, S.-P. & Miller, A. J. The interplay of internal and forced modes of Hadley cell expansion: Lessons from the global warming hiatus. *Clim. Dyn.* **51**, 305–319 (2018).
33. Zhou, W., Xie, S.-P. & Yang, D. Enhanced equatorial warming causes deep-tropical contraction and subtropical monsoon shift. *Nat. Clim. Chang.* **9**, 834–839 (2019).
34. Menzel, M. E., Waugh, D. & Grise, K. Disconnect between Hadley cell and subtropical jet variability and response to increased CO2. *Geophys. Res. Lett.* **46**, 7045–7053 (2019).
35. Hu, D., Guo, Y.-P., Tan, Z.-M. & Guan, Z. Interannual relationship between the boreal spring arctic oscillation and the northern hemisphere Hadley circulation extent. *J. Clim.* **32**, 4395–4408 (2019).
36. Thompson, D. W. & Wallace, J. M. Annular modes in the extratropical circulation. Part I: month-to-month variability. *J. Clim.* **13**, 1000–1016 (2000).
37. Thompson, D. W., Wallace, J. M. & Hegerl, G. C. Annular modes in the extratropical circulation. Part II: trends. *J. Clim.* **13**, 1018–1036 (2000).
38. Vallis, G. K., Gerber, E. P., Kushner, P. J. & Cash, B. A. A mechanism and simple dynamical model of the north Atlantic oscillation and annular modes. *J. Atmos. Sci.* **61**, 264–280 (2004).
39. Chen, S., Yu, B. & Chen, W. An analysis on the physical process of the influence of AO on ENSO. *Clim. Dyn.* **42**, 973–989 (2014).
40. Kang, S. M. & Polvani, L. M. The interannual relationship between the latitude of the eddy-driven jet and the edge of the Hadley cell. *J. Clim.* **24**, 563–568 (2011).
41. Staten, P. W. & Reichler, T. On the ratio between shifts in the eddy-driven jet and the Hadley cell edge. *Clim. Dyn.* **42**, 1229–1242 (2014).
42. Solomon, A., Polvani, L., Waugh, D. & Davis, S. Contrasting upper and lower atmospheric metrics of tropical expansion in the Southern Hemisphere. *Geophys. Res. Lett.* **43**, 10496–10503 (2016).
43. Davis, N. & Birner, T. On the discrepancies in tropical belt expansion between reanalyses and climate models and among tropical belt width metrics. *J. Clim.* **30**, 1211–1231 (2017).
44. Waugh, D. W. et al. Revisiting the relationship among metrics of tropical expansion. *J. Clim.* **31**, 7565–7581 (2018).

45. D'Agostino, R., Scambiati, A. L., Jungclaus, J. & Lionello, P. Poleward shift of northern subtropics in winter: time of emergence of zonal versus regional signals. *Geophys. Res. Lett.* **47**, e2020GL089325 (2020).
46. Nguyen, H., Evans, A., Lucas, C., Smith, I. & Timbal, B. The Hadley circulation in reanalyses: climatology, variability, and change. *J. Clim.* **26**, 3357–3376 (2013).
47. Byrne, M. P. & Schneider, T. Narrowing of the ITCZ in a warming climate: physical mechanisms. *Geophys. Res. Lett.* **43**, 11350–11357 (2016).
48. Caballero, R. Role of eddies in the interannual variability of Hadley cell strength. *Geophys. Res. Lett.* **34**, L22705 (2007).
49. Singh, M. S. & Kuang, Z. Exploring the role of eddy momentum fluxes in determining the characteristics of the equinoctial Hadley circulation: Fixed-SST simulations. *J. Atmos. Sci.* **73**, 2427–2444 (2016).
50. Ceppi, P. & Hartmann, D. L. On the speed of the eddy-driven jet and the width of the Hadley cell in the southern hemisphere. *J. Clim.* **26**, 3450–3465 (2013).
51. Hoskins, B. J. & Hodges, K. I. New perspectives on the Northern Hemisphere winter storm tracks. *J. Atmos. Sci.* **59**, 1041–1061 (2002).
52. Chang, E. K., Lee, S. & Swanson, K. L. Storm track dynamics. *J. Clim.* **15**, 2163–2183 (2002).
53. Phillips, N. A. Energy transformations and meridional circulations associated with simple baroclinic waves in a two-level, quasi-geostrophic model. *Tellus* **6**, 273–286 (1954).
54. Chemke, R. & Polvani, L. M. Exploiting the abrupt 4×CO_2 scenario to elucidate tropical expansion mechanisms. *J. Clim.* **32**, 859–875 (2019).
55. Tandon, N. F., Gerber, E. P., Sobel, A. H. & Polvani, L. M. Understanding Hadley cell expansion versus contraction: Insights from simplified models and implications for recent observations. *J. Clim.* **26**, 4304–4321 (2013).
56. Randel, W. J. & Held, I. M. Phase speed spectra of transient eddy fluxes and critical layer absorption. *J. Atmos. Sci.* **48**, 688–697 (1991).
57. Chen, G. & Held, I. M. Phase speed spectra and the recent poleward shift of southern hemisphere surface westerlies. *Geophys. Res. Lett.* **34**, L21805 (2007).
58. Chen, G., Lu, J. & Frierson, D. M. W. Phase speed spectra and the latitude of surface westerlies: Interannual variability and global warming trend. *J. Clim.* **21**, 5942–5959 (2008).
59. Robinson, W. A. On the midlatitude thermal response to tropical warmth. *Geophys. Res. Lett.* **29**, 1190 (2002).
60. Seager, R., Harnik, N., Kushnir, Y., Robinson, W. & Miller, J. Mechanisms of hemispherically symmetric climate variability. *J. Clim.* **16**, 2960–2978 (2003).
61. Ambaum, M. H., Hoskins, B. J. & Stephenson, D. B. Arctic oscillation or North Atlantic oscillation? *J. Clim.* **14**, 3495–3507 (2001).
62. Hu, Y. & Zhou, C. Decadal changes in the Hadley circulation. *Adv. Geosci. Atmos. Sci.* **16**, 61–74 (2010).
63. Holton, J. R. & Tan, H.-C. The influence of the equatorial quasi-biennial oscillation on the global circulation at 50 mb. *J. Geophys. Res. Atmos.* **37**, 2200–2208 (1980).
64. Haigh, J. D., Blackburn, M. & Day, R. The response of tropospheric circulation to perturbations in lower-stratospheric temperature. *J. Clim.* **18**, 3672–3685 (2005).
65. Xia, Y. et al. Significant contribution of stratospheric water vapor to the poleward expansion of the Hadley circulation in autumn under greenhouse warming. *Geophys. Res. Lett.* **48**, e2021GL094008 (2021).
66. Hoskins, B. J. & Yang, G.-Y. The detailed dynamics of the Hadley cell. Part II: December–February. *J. Clim.* **34**, 805–823 (2021).
67. Hersbach, H. et al. The ERA5 global reanalysis. *Q. J. R. Meteorol. Soc.* **146**, 1999–2049 (2020).
68. Rayner, N. et al. Global analyses of sea surface temperature, sea ice, and night marine air temperature since the late nineteenth century. *J. Geophys. Res. Atmos.* **108**, 4407 (2003).
69. Son, S.-W. & Lee, S. The response of westerly jets to thermal driving in a primitive equation model. *J. Atmos. Sci.* **62**, 3741–3757 (2005).
70. Hayashi, Y. A generalized method of resolving disturbances into progressive and retrogressive waves by space Fourier and time cross-spectral analyses. *J. Meteorol. Soc. Jpn.* **49**, 125–128 (1971).
71. Taylor, K. E., Stouffer, R. J. & Meehl, G. A. An overview of CMIP5 and the experiment design. *Bull. Am. Meteorol. Soc.* **93**, 485–498 (2012).

ACKNOWLEDGEMENTS

This work is supported by a National Research Foundation of Korea (NRF) grant funded by the Korean government (MSIP) (No. NRF-2020R1A2C2009414) and Learning & Academic research institution for Master's PhD students and Postdocs (LAMP) Program of the National Research Foundation of Korea (NRF) grant funded by the Ministry of Education (No. RS-2023-00301938). J.L. is supported by the US Department of Energy Office of Science as part of the Regional and Global Model Analysis (RGMA) Program Area. The Pacific Northwest National Laboratory (PNNL) is operated for DOE by the Battelle Memorial Institute under contract DE-AC05-76RLO1830. Y.H. is supported by the National Natural Science Foundation of China under grant 41888101. P.W.S. is funded by the NSF grant (No. 2140235): Observing and Modeling the Upper-Troposphere-Lower-Stratosphere Moistening Processes across Scales.

AUTHOR CONTRIBUTIONS

K.-H.S., S.-P.Y., J.L., and Y.H. designed the initial research framework. P.W.S. and D.M.W.F. provide additional ideas and deeper insights. Technical analysis was conducted by K.-H.S. and S.-P.Y. J.L. and P.W.S. contributed to the creation of Figs. 3, 6, and 10. All authors contributed to the result analysis, interpretation, and writing.

COMPETING INTERESTS

The authors declare no competing interests.

ADDITIONAL INFORMATION

Supplementary information The online version contains supplementary material available at https://doi.org/10.1038/s41612-023-00533-w.

Correspondence and requests for materials should be addressed to Kyong-Hwan Seo or Paul W. Staten.

Reprints and permission information is available at http://www.nature.com/reprints

Publisher's note Springer Nature remains neutral with regard to jurisdictional claims in published maps and institutional affiliations.